Multidimensional geometric aspects of the solid–liquid transition in simple substances

Randall A. LaViolette and Frank H. Stillinger

AT&T Bell Laboratories, Murray Hill, New Jersey 07974

Any molecular system explores significantly different regions of the potential-energy hypersurface as the system is found, respectively, in the solid and liquid phases. We study in detail the multidimensional geometry of these different regions with molecular-dynamics calculations for 256 simple atoms in a fixed volume. The atomic interactions are chosen to represent the noble gases. The stable crystal for this model displays a face-centered cubic structure. We evaluate the local gradient and curvatures of the regions of the hypersurface sampled by the system for a wide range of temperatures. We observe that a significant fraction of the curvatures become negative in the region sampled by the system at temperatures even as low as one-fourth the melting temperature. Further, the curvature distribution changes dramatically with respect to temperature at the melting point. We also construct and evaluate a new distribution for the distance between the atoms in their instantaneous dynamical configurations and those in their corresponding "quenched" configuration (i.e., the configuration found at the corresponding potential-energy minimum). With the help of this new distribution, we conclude that the quenched configurations which are encountered during the melting process are structures which contain vacancy-interstitial defect pairs.

I. INTRODUCTION

We propose to investigate the transition between liquid and solid phases in terms of the topography of those thermodynamically predominant portions of the potential-energy hypersurface for N molecules with varying temperature T but fixed density. In what follows, we explain why an investigation of the topography of $U(\mathbf{r}_1 \ldots \mathbf{r}_N)$ (the potential energy hypersurface expressed as a function of the coordinates $\mathbf{r}_1 \ldots \mathbf{r}_N$ of the N molecules contained in a fixed volume V), should produce useful information about the solid–liquid transition. We then present: the parameters with which we monitor the shape of the potential-energy hypersurface; the molecular dynamics calculation of the parameters for the potential-energy surface of $N = 256$ argon-like atoms, at a fixed density but over a wide range of temperatures; and a presentation of the results. We conclude with a discussion of the consequences of these results for some previously proposed melting theories, and of what future use one might make of our results. The treatment here is entirely classical, and so, e.g., our comments about the low-temperature behavior of our system must be taken in that context. Further, since we only consider phases which are stable at equilibrium, we exclude the formation of glasses from our discussion.

We expect at the outset that the topographical differences between the region of $U(\mathbf{r}_1 \ldots \mathbf{r}_N)$ occupied by liquid-phase configurations and the region occupied by solid-phase configurations should be so characteristic and pronounced that it should be relatively straightforward to choose local geometric parameters which will clearly and always signal the phase transition as the temperature passes through the transition temperature. The portion of $U(\mathbf{r}_1 \ldots \mathbf{r}_N)$ sampled by the equilibrium configurations in the low-temperature solid phase is one of the permutationally equivalent wells whose sole minimum, at $\mathbf{r}_1^0 \ldots \mathbf{r}_N^0$, is the static crystal energy U_0, and is also a global minimum of $U(\mathbf{r}_1 \ldots \mathbf{r}_N)$. For low enough temperatures, the configurations primarily sample only the harmonic region about the absolute minimum. There the hypersurface, and also the thermodynamics, can be completely characterized by the well depth $U(\mathbf{r}_1^0 \ldots \mathbf{r}_N^0)$, and the local curvature tensor $\nabla\nabla U(\mathbf{r}_1^0 \ldots \mathbf{r}_N^0)$. On the other hand, at the higher temperatures of the liquid phase, the configurations sample a much more complicated and anharmonic region of $U(\mathbf{r}_1 \ldots \mathbf{r}_N)$. This region is shaped by many minima, maxima, and saddle points which induce a wide variety of both convex and concave contours on the hypersurface (as portrayed schematically in Fig. 1), features which are not present in the portion sampled by the harmonic solid. As observed in earlier work,[1] this suggests that we can partition $U(\mathbf{r}_1 \ldots \mathbf{r}_N)$ uniquely into distinct regions so that each region is a "basin" whose "drainage lines" descend toward exactly one of the minima. If the system melts, then the configurations will no longer be constrained to sample only the basin surrounding the crystal minimum, but will be free to sample a wide variety of higher-lying basins. Therefore the list of attributes of the hypersurface which would change dramatically upon melting or freezing should include not only the local slopes and curvatures of $U(\mathbf{r}_1 \ldots \mathbf{r}_N)$ but also the depths and apertures of the basins of $U(\mathbf{r}_1 \ldots \mathbf{r}_N)$ which would be encountered by the trajectory. In the next section we present our choice of parameters corresponding to these attributes. Although these parameters are presented in the context of a molecular dynamics calculation,[2] where the configurations $\mathbf{r}_1(t) \ldots \mathbf{r}_N(t)$ are generated by the classical equations of motion at every time step t, the same considerations would apply if the configurations were generated by, say a Monte Carlo calculation.[2]

II. THE PARAMETERS

We consider first the local slope and curvature of the hypersurface which the configurations encounter at any in-
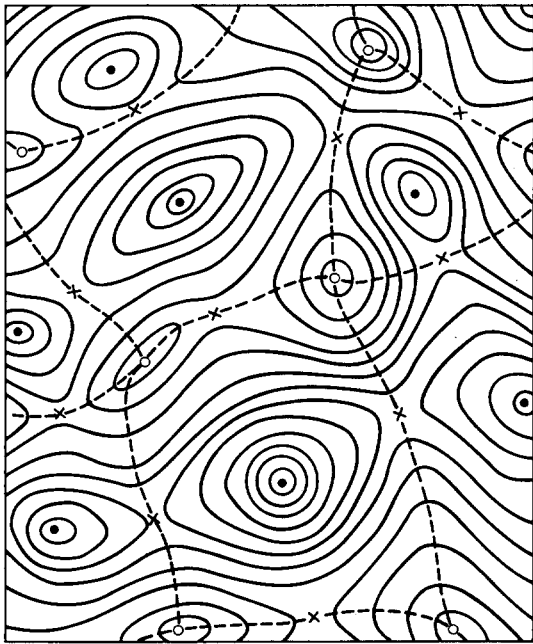
FIG. 1. Schematic representation of the potential-energy hypersurface. Open circles are maxima, solid circles are minima. Saddle points are indicated by crosses. The solid curves are equipotential loci. Dotted curves passing through saddle points and converging at maxima represent boundaries of the steepest-descent basins that surround each local minimum.

stant t. In general they are given by, respectively, the gradient $\nabla U[\mathbf{r}_1(t) ... \mathbf{r}_N(t)]$ and the Hessian $\nabla\nabla U[\mathbf{r}_1(t) ... \mathbf{r}_N(t)]$. However, these arrays contain much more information than we can use, so we focus on parameters which contract the information into a more compact form. We therefore monitor the local slope with the square of the (Euclidean) norm of the gradient, $|\nabla U[\mathbf{r}_1(t) ... \mathbf{r}_N(t)]|^2$. To monitor the curvature, we merely count the number of negative eigenvalues of $\nabla\nabla U[\mathbf{r}_1(t) ... \mathbf{r}_N(t)]$. The appearance of negative eigenvalues in the Hessian signals the entry of the trajectory into a nonconvex portion of the hypersurface.

Next, we consider the depth and aperture of the basin in which the configuration is found at any time. To find the minimum of the basin, we can cut across the contours from any point in the basin down to the minimum with, e.g., a steepest-descent or conjugate-gradient procedure. Such procedures have been employed successfully for this purpose in earlier work.[3] With the resulting quenched configuration $\mathbf{r}_1^q ... \mathbf{r}_N^q$, we calculate two parameters: the quench energy $U_q = U(\mathbf{r}_1^q ... \mathbf{r}_N^q)$, corresponding to the depth of the minimum, and the "return-distance" (squared) $\delta r_q^2(t) = (1/N) \times \Sigma_{i=1}^N |\mathbf{r}_i(t) - \mathbf{r}_i^q|^2$. The average of $\delta r_q^2(t)$ over all configurations in that basin gives, for each basin, an estimate of the aperture of that portion of the basin encountered by the trajectories. When the system is in the undefective solid phase, then the basin is the well about the crystal (global) minimum U_0, and the average return distance (squared) is identical with the average displacement (squared) parameter used in the venerable Lindemann melting theory. We discuss the Lindemann theory in detail in the Conclusion. For now, we observe that the average over all configurations is a straight-

forward generalization, for both the solid and liquid phase, of Lindemann's displacement parameter for the solid phase.

III. THE MOLECULAR-DYNAMICS CALCULATION

We study the melting of $N = 256$ atoms which interact via the pair potential

$$u(r) = A(r^{-12} - r^{-5})\exp[(r-a)^{-1}], \qquad 0 < r < a,$$

$$= 0, \qquad r \geqslant a.$$

The parameter a fixes the length of the interaction, so that the attraction is smoothly truncated to zero at $r = a$. The parameters A and a were chosen so that $u(1) = 0$ and at the minimum $u(r_e) = -1$, and so, $A = 6.767\,441$ and $a = 2.464\,918\,32$. Then we can view $u(r)$ as a smoothly cutoff version of the Lennard-Jones potential[2] in the reduced units $\epsilon = 1$ and $\sigma = 1$. Figure 2 displays $u(r)$ compared with the Lennard-Jones potential in the reduced units. The potential $u(r)$ has been discussed by Stillinger and Weber,[3] and has two noteworthy advantages. First, the attractions smoothly vanish at less than three atomic diameters away from the center of the atom. Second, the static crystal lattice has a face-centered cubic structure for a range of densities where the zero-temperature pressure is positive. This property is not shared by, e.g., the popular Lennard-Jones potential, which produces a hexagonal close-packed lattice at $T = 0$ for all densities where the pressure is positive.[4] Not only is the face-centered cubic structure more symmetric than the hexagonal close-packed structure, but also it is the crystal structure experimentally observed for rare gas solids.[4] Figure 3(a) shows our calculated static crystal energy for the atoms in the face-centered cubic and the hexagonal close-packed lattices, as a function of v, the volume per atom. Figure 3(b) shows the difference between the energies corresponding to the two structures. For $v \leqslant 0.937\,85$, the zero temperature
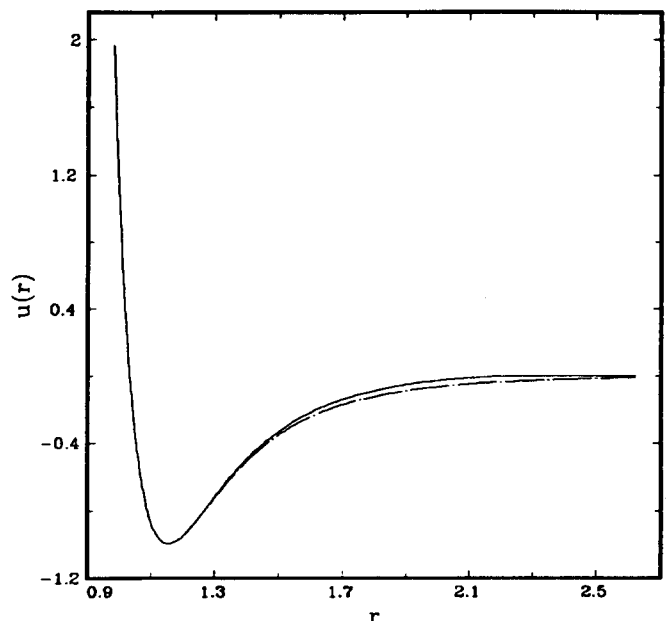

FIG. 2. The model pair-potential (solid curve) and the Lennard-Jones pair potential (chain-dot curve) as a function of interatomic radius, in reduced units. Both functions vanish at $r = 1$ and pass through minima (-1) at $r_e = 2^{1/6}$.
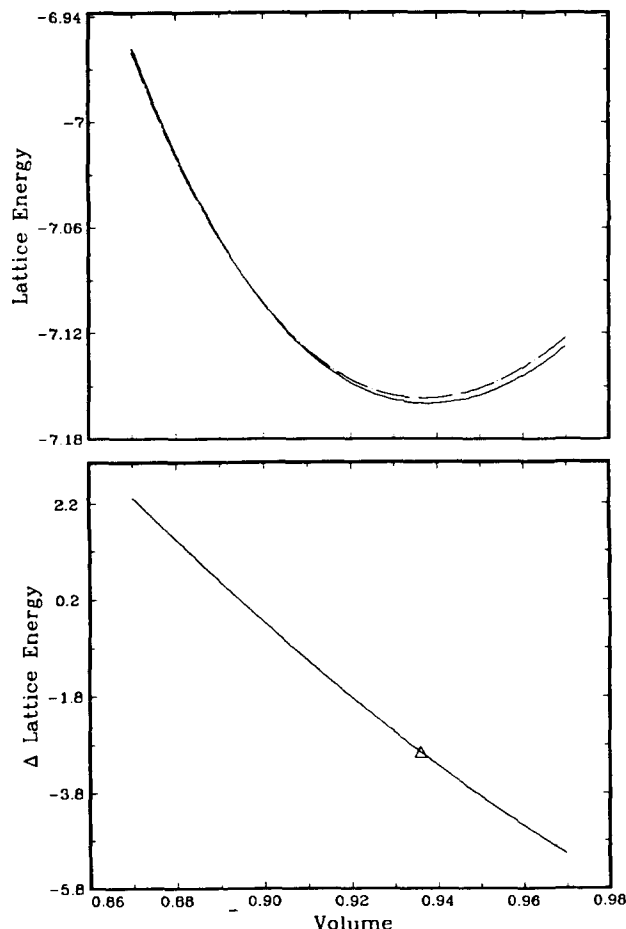
FIG. 3. The upper panel (a) shows the $T = 0$ lattice energy as a function of volume per atom for the face-centered cubic lattice (solid curve) and the hexagonal close-packed lattice (chain-dot curve). The lower panel (b) shows the energy difference $\Delta = (U_{fcc} - U_{hcp}) \times 1000$. The triangle in panel (b) marks the volume per atom which we chose for the molecular dynamics calculation.

pressure is positive. In this range, the face-centered cubic structure is preferred for atomic volumes as low as $\nu = 0.8900$, while the hexagonal close-packed structure is preferred for lower ν.

We initiate the molecular dynamics calculation by placing the N atoms in a face-centered cubic lattice which fits in a cube with volume $(6.215\ 238\ 272)^3$, so that the volume per atom, $\nu = 0.937\ 85$ corresponds to the minimum static crystal energy $U_0 = -1833.4918$. The dimensions of the cell are fixed throughout the calculation, and periodic boundary conditions are imposed.[2] The classical equations of motion are solved with a fifth-order Gear algorithm.[5] The time step Δt ranges from $\Delta t = 0.0125$ for temperatures below melting to $\Delta t = 0.0025$ for the high temperature liquid, in our reduced units for atoms of unit mass. With these choices, the total energy was conserved to at least one part in 10^5 over each run. We measure time in multiples of $\tau = 0.0125$. All the states discussed in the next section, with temperatures ranging from $T = 0.5$ to $T = 6.2$, were produced by increasing the last instantaneous momenta of the previous state by between 5% and 50%, and advancing the trajectory by 1500τ before collecting averages. We calculate $\langle P \rangle$, the time average of some parameter P, over trajectories at least

10 000τ long. We calculated the temperature,[6] pressure, and potential energy of the system every 10τ. To find $\langle |\nabla U [\mathbf{r}_1(t) \dots \mathbf{r}_N(t)]|^2 \rangle^{1/2}$, we collected the sum

$$\sum_{i=1}^{N} \sum_{k=x,y,z} (f_i^k(t))^2,$$

where $f_i^k(t)$ is the k th component of the force on atom i due to all the other atoms at time t. At every 200τ we calculated the eigenvalues of $\nabla\nabla U [\mathbf{r}_1(t) \dots \mathbf{r}_N(t)]$. The components of the Hessian are

$$h_{i\alpha j\gamma} = \frac{-\delta_{\alpha\gamma}}{r_{ij}} \frac{du(r_{ij})}{dr} - \frac{(r_{i\alpha} - r_{j\alpha})(r_{i\gamma} - r_{j\gamma})}{r_{ij}}$$

$$\times \frac{d}{dr}\left(\frac{1}{r}\frac{du(r_{ij})}{dr}\right) \quad (i \neq j),$$

$$h_{i\alpha i\gamma} = -\sum_{i \neq j} h_{i\alpha j\gamma},$$

where α and γ label the components of the coordinates of atoms i and j, $r_{ij} = |\mathbf{r}_i(t) - \mathbf{r}_j(t)|$, and $\delta_{\alpha\gamma}$ is the Kronecker delta. At every 100τ we quenched the instantaneous configuration $\mathbf{r}_1(t) \dots \mathbf{r}_N(t)$ with a steepest-descent procedure[3] to find $\mathbf{r}_1^q \dots \mathbf{r}_N^q$, the corresponding configuration at the minimum of the basin, and evaluated $U(\mathbf{r}_1^q \dots \mathbf{r}_N^q)$, and δr_q^2. We also scored the frequency of single-atom return distances in order to form the probability distribution function $P(r^2)$ $= \langle \frac{1}{N}\sum_{i=1}^{N} \delta(r^2 - |r_i(t) - r_i^q|^2) \rangle$, where $\delta(x)$ is the one-dimensional Dirac delta function.

IV. RESULTS

Figure 4 shows our calculated average potential energy $\langle U \rangle$ for temperatures from $T = 0$ to $T = 6.2$. The break in the curve indicates that the solid melts at $T_m = 2.40 \pm 0.05$. The melting temperature at this density is comparable to that found for the Lennard-Jones solid.[7] We also found that the pressures were always positive, and increased with temperature, and exhibited a characteristic break at T_m.
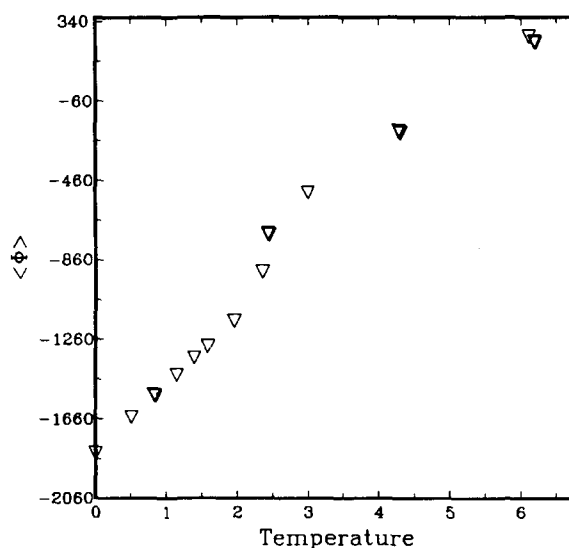

FIG. 4. The average potential energy $\langle \Phi \rangle$ as a function of temperature, showing the melting of the model solid.

The root-mean square of the norm of the gradient, $\langle |\nabla U [\mathbf{r}_1(t) \dots \mathbf{r}_N(t)]|^2 \rangle^{1/2}$, is by itself a measure of the average local slope of the hypersurface at the given total energy. However, we present instead, in Fig. 5, the calculated values for

$$\left(\frac{1}{3NT} \langle |\nabla U [\mathbf{r}_1(t) \dots \mathbf{r}_N(t)]|^2 \rangle \right)^{1/2}.$$

In the limit of $T = 0$, this is ω_E, the classical Einstein frequency of the crystal,[8] defined by

$$\omega_E^2 = \frac{1}{3N} \text{tr } \nabla\nabla U(\mathbf{r}_1^0 \dots \mathbf{r}_N^0).$$

For higher temperatures, the average $1/3NT \langle |U [\mathbf{r}_1(t) \dots \mathbf{r}_N(t)]|^2 \rangle$ can be interpreted as a generalized Einstein frequency squared,[9] which we denote by Ω_E^2. However, Ω_E^2 corresponds to the average of tr $\nabla\nabla U [\mathbf{r}_1(t) \dots \mathbf{r}_N(t)]$ evaluated at the instantaneous configurations rather than at the crystal minimum. We observe that the $T = 0$ intercept of the curve in Fig. 5 is precisely the conventional Einstein frequency by calculating directly tr $\nabla\nabla U(\mathbf{r}_1^0 \dots \mathbf{r}_N^0)$ for the static crystal lattice. The ω_E calculated in this way is also shown in Fig. 5, and does indeed agree with our (graphical) estimate of $\lim_{T \to 0} \Omega_E$. We should expect that Ω_E would decrease with increasing temperature if the crystal were permitted to expand in our calculation. However, the volume is fixed in our calculation, and so we expect and see that Ω_E increases with temperature. Several theories of melting identify T_m with the temperature at which the Einstein frequency of the crystal ω_E becomes complex.[10] Such approaches ignore the existence of the coexisting liquid phase. While Ω_E remains real at all temperatures, we observe that the curve of the calculated Ω_E suffers a sharp break at T_m, where Ω_E discontinuously increases by about 10%. Further, Ω_E is well defined in the liquid phase and contains information about the liquid

phase. Although Ω_E cannot be calculated easily by the self-consistent phonon techniques which have been used to calculate ω_E, the fact that Ω_E signals so clearly the solid–liquid phase transitions may be illuminating to those who study melting as a phonon instability in the crystal.

Figure 6 shows our calculated $\langle$No. $\sigma\rangle$, the average number of *negative* eigenvalues of $\nabla\nabla U [\mathbf{r}_1(t) \dots \mathbf{r}_N(t)]$, expressed as a percentage of all the $3(N-1)$ nonzero eigenvalues. For very low temperatures, $\langle$No. $\sigma\rangle$ should remain zero, and this is evidently the case for $T < 0.5$. However, near $T = 0.52$, $\langle$No. $\sigma\rangle$ suddenly rises along an eventually concave curve, until the curve suffers a break at T_m. The jump in $\langle$No. $\sigma\rangle$ is from about 17% to 20%. Above T_m, $\langle$No. $\sigma\rangle$ follows, within the statistical error, a rising and slightly concave curve over the temperature range examined.

Figure 7 shows our calculated $\langle \delta r_q^2 \rangle^{1/2}$, the root-mean square return distance averaged over all configurations. For low temperatures, $\langle \delta r_q^2 \rangle^{1/2}$ increases with $T^{1/2}$, as expected,[11] but above T_m, the curve appears to increase linearly with temperature. The curve shows a sharp break at T_m.

Of the two calculated states nearest T_m, one is unambiguously a liquid at $T = 2.43$, and has a root-mean square return distance of $\langle \delta r_q^2 \rangle^{1/2} = 0.45$. The other is a defective solid at $T = 2.35$, with $\langle \delta r_q^2 \rangle^{1/2} = 0.27$. Regrettably, a comparison of the usual radial distribution function of the solid at $T = 2.35$ with those of the solids at the lower temperatures does not reveal any important differences between the solids. However, a projection of the sequence of instantaneous return distances $\delta r_q(t) = + (\delta r_q^2)^{1/2}$ and the corresponding quench energies $U_q [\mathbf{r}_1(t) \dots r_N(t)]$ into the $(\delta r_q, U_q)$ plane shows very clearly that the defective configurations occupy a topographically distinct region of $U(\mathbf{r}_1 \dots \mathbf{r}_N)$. Figure 8 shows the projection δr_q vs U_q for, respectively, the solid at $T = 1.96$, the solid at $T = 2.35$, the liquid at $T = 2.43$, and
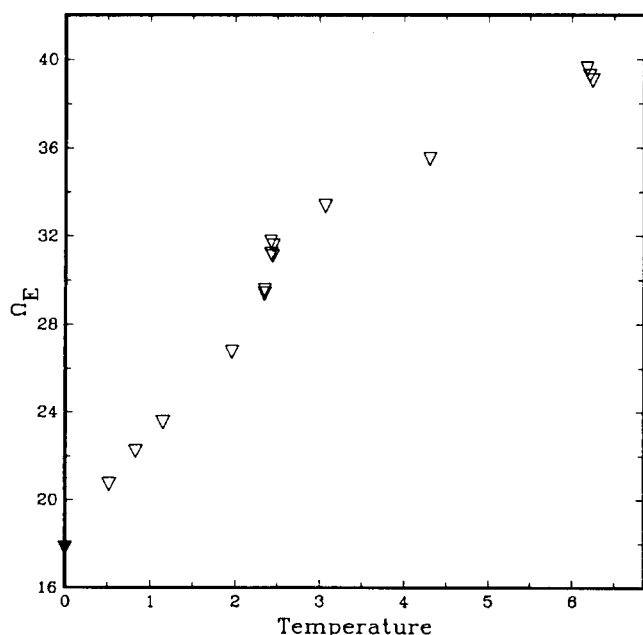

FIG. 5. The generalized Einstein frequency Ω_E as a function of temperature. The solid triangle at $T = 0$ represents the conventional Einstein frequency for the model solid, which was calculated directly from the trace of the force-constant matrix evaluated at the static crystal configuration.
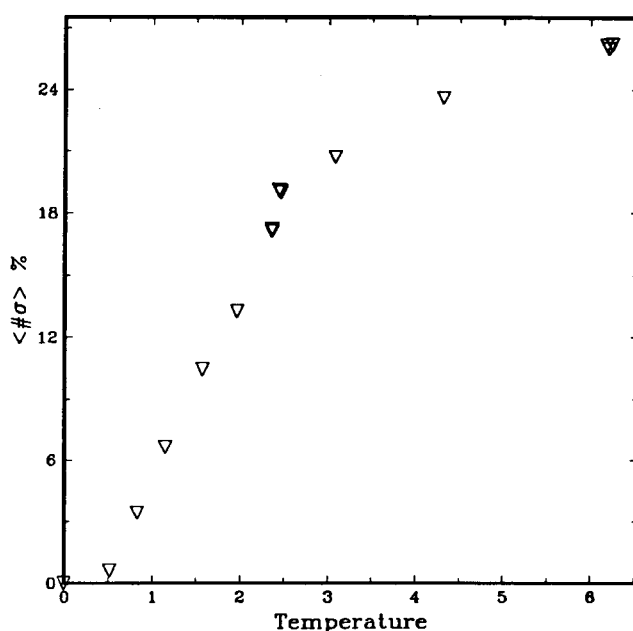

FIG. 6. The average number of negative eigenvalues of the force-constant matrix (evaluated at the instantaneous dynamical configurations), expressed as the percentage of the $3(N-1)$ total nonzero eigenvalues, and displayed as a function of temperature.
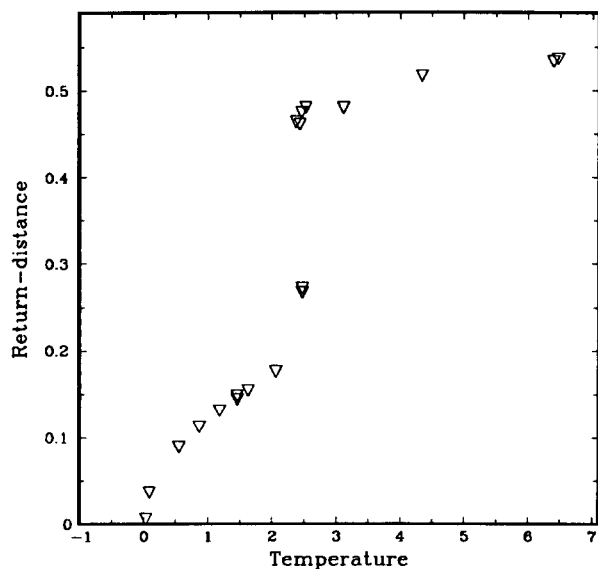
FIG. 7. The root-mean square return distance $\langle \delta r_q^2 \rangle^{1/2}$ as a function of temperature.

the liquid at $T = 6.2$. At $T = 1.96$, the configurations are (statistically) still confined to the well about the crystal minimum U_0. For the solid at $T = 2.35$, the configurations occupy alternately the basin about U_0 and basins about the minima with mean depth $U_q^* = -1796.77$. The liquids at $T = 2.43$ and $T = 2.66$ show no such simple dichotomy between minima, for here the configurations sample a portion of the hypersurface contained in a wide variety of basins, whose minima are each distinctly above U_q^*.

In Fig. 8(b), corresponding to the solid at $T = 2.35$, the quench energies clustered about U_q^* each appear to be equal to U_q^*. Actually they are each different from U_q^*. To resolve more clearly the energy differences between the minima about U_q^*, we show those minima drawn on a more expand-

ed energy scale in Fig. 9. We can distinguish, to eight decimal places, between 12 distinct wells of varying depth, from among the 43 quenched configurations clustered about U_q^*. We suppose that the quenched configurations each correspond to a face-centered cubic lattice with a single vacancy-interstitial defect pair, differing primarily according to the orientation of the defects with respect to the crystal axes, and to each other. To support this conjecture, we created, in an independent calculation, a vacancy-interstitial defect pair with a small separation in the static ($T = 0$) face-centered cubic lattice, and subsequently allowed the system to relax at low temperatures via molecular dynamics. We quenched the relaxed configuration to find the potential energy of the defective lattice $U^{v-i} = -1796.8813$, very near one of the observed quench energies ($U_q = -1796.8976$) and also near the lowest ($U_q = -1797.0642$) of the 12 quench energy classes portrayed in Fig. 9.

Finally, Figs. 10 and 11 show $P(r^2)$, our calculated frequency distributions of the single-atom return distances, for the same temperatures used in Fig. 8. When the solid melts, $P(r^2)$ broadens, which again indicates that the configurations in the liquid phase encounter a topographically distinct and more diverse region of the hypersurface than those in the solid phase. Not only the shape but also the functional form of $P(r^2)$ changes. To show this, we attempted to fit $P(r^2)$ to the Einstein prediction $P_E(r^2)dr^2 = Ar \exp(-ar^2)dr^2$, where A and a are constants determined by a least-squares fit of the observed $P_E(r^2)$ to $P(r^2)$. Even at temperatures as high as $T = 1.96$, $P_E(r^2)$ is an excellent fit to the data. However, at $T = 2.35$, and for all higher temperatures, the function $P_E(r^2)$ can no longer be made to fit the data in a reasonable way.[12] This indicates a basic change in the functional form of $P(r^2)$ as the system begins to melt. In particular, we find that $P(r^2)$ in the liquid phase has a more extended tail at large r^2 than can be accommodated by any scaled version of P_E.
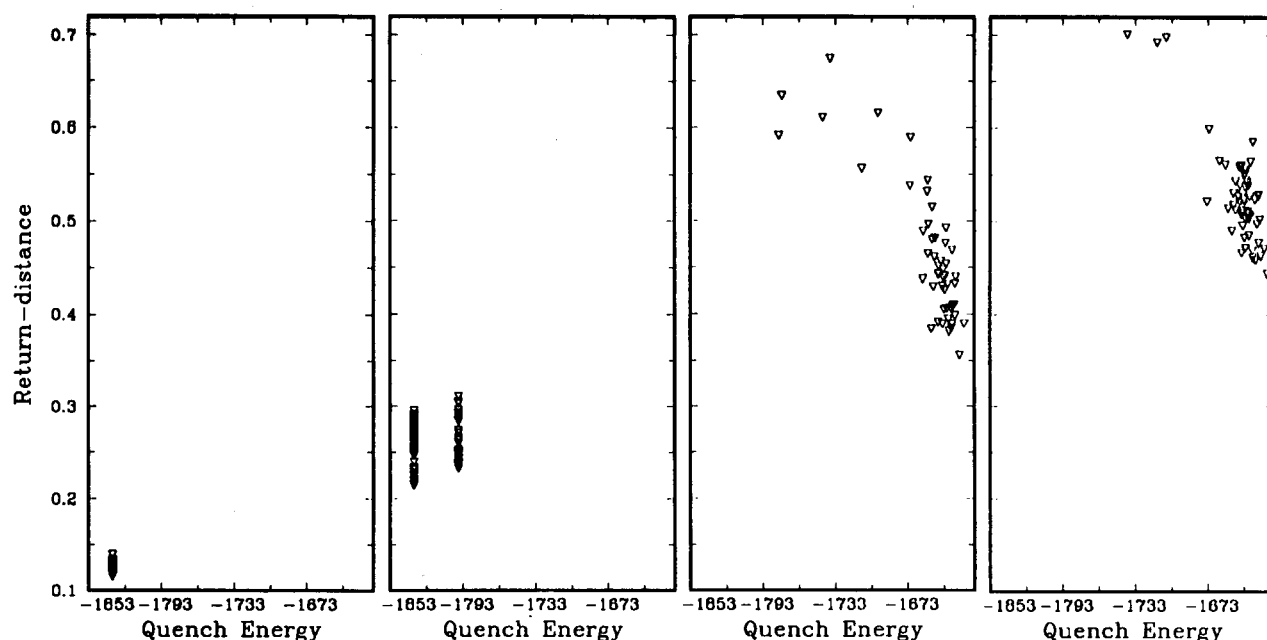

FIG. 8. Projection of the instantaneous quench energies U_q and the corresponding return distances δr_q for (from left to right) $T = 1.92$ (a), $T = 2.35$ (b), $T = 2.43$ (c), $T = 2.66$ (d).
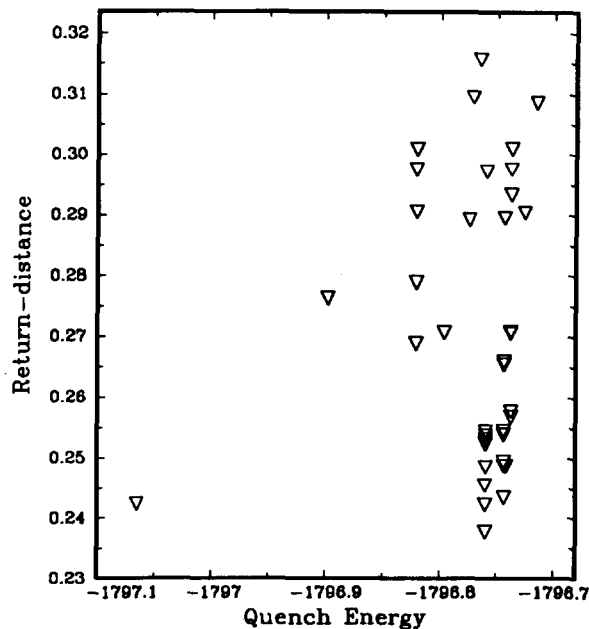
FIG. 9. A portion of Fig. 8(b) on an expanded scale.

FIG. 11. $P(r^2)$ as a function of r^2. The solid curve corresponds to $T = 2.43$, the dashed curve to $T = 6.2$. The vertical scale shows the normalized frequencies multiplied by 1000. Both noisy curves were partially smoothed by a least-squares fit to a sequence of cubic polynomials in order to see clearly the differences between the two curves for $r^2 > 0.2$

V. CONCLUSIONS

The results displayed in Figs. 4 through 11 show that the topographical differences between the portions of $U(\mathbf{r}_1 \ldots \mathbf{r}_N)$ sampled by configurations in the liquid and solid phases are indeed dramatic. By exploring the aperture and depth of the basins which partition the hypersurface we are able to portray the transition between solid and liquid phases as follows. In the solid phase, upon heating from $T = 0$, the configurations very quickly begin to sample anharmonic regions of the potential-energy well about the crystal minimum, as seen in Fig. 6. Nevertheless, as Fig. 8 shows, the configurations for our $N = 256$ system are confined to that well for temperatures up to nearly T_m. At T_m, the configurations are finally able to invade regions contained in many basins of diverse slope, curvature, aperture, and depth. As Figs. 8(c) and 8(d) show, the configurations sample that part of the hypersurface contained in basins which are wider and shallower than the well about the crystal minimum. Further, the
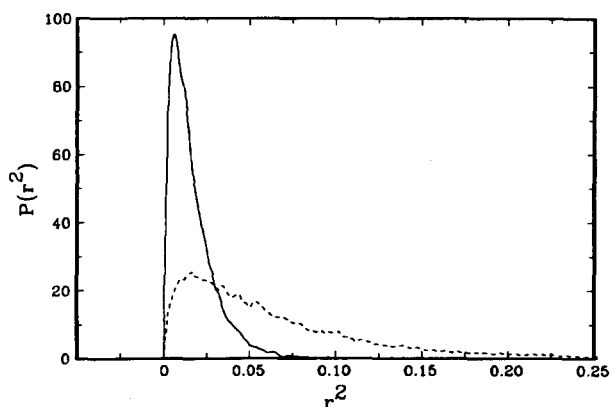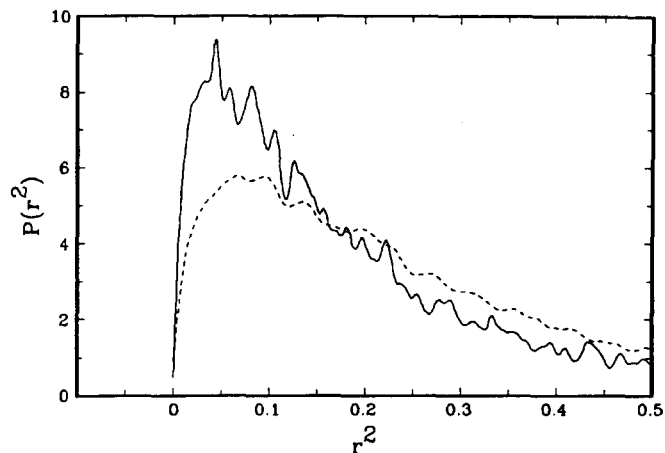
region that they sample in the liquid phase is apparently contained in virtually the same population of basins for all temperatures above T_m. This may also be demonstrated by comparing the radial distribution functions of the quenched configurations found at different temperatures above T_m. These radial distribution functions also appear to be independent of temperature,[13] consistent with results shown in Fig. 8. The minima of these basins may thus be called the "inherent structures" of the liquid, because they identify the basins which contain the region of $U(\mathbf{r}_1 \ldots \mathbf{r}_N)$ sampled by the configurations. The term inherent structures, introduced in earlier work by Stillinger and Weber,[1,3] should not be viewed as an attempt to represent the liquid as a solid-like entity, as does the "significant-structure" theory of Eyring and others.[14] As we have emphasized in this work, the point of view expressed by the term inherent structures assumes dramatic and basic differences between configurations in the solid and liquid phases, for otherwise we could not expect to extract useful information about the liquid–solid transition by studying these inherent structures and the topography of the potential-energy hypersurface. This work demonstrates that the liquid and solid phases are indeed distinguished by gross topographical differences in the hypersurface, and to that extent, we can offer no support for the significant-structures picture of liquids.

As we mentioned in the Introduction, the root-mean square return distance $\langle \delta r_q^2 \rangle^{1/2}$ is a straightforward generalization of the Lindemann displacement parameter $\langle \delta u^2 \rangle^{1/2}$, which measures the root-mean square displacement of the atoms in the solid from the static crystal configuration.[15–17] The Lindemann theory of melting asserts that upon heating, the solid melts when $\langle \delta u^2 \rangle^{1/2}$ reaches a certain maximum permissible fraction of the lattice spacing, and that this maximum is constant for all melting densities and temperatures. This assertion is exact for atoms which interact according to the pair potential $u(r) = \text{const} \times r^{-n}$, for then the energy and distance scale together.[15–17] Many atomic systems which do not interact in this manner nevertheless also appear to conform to the Lindemann picture of melting. For a

FIG. 10. The atomic return distance frequency distribution $P(r_2)$ as a function of r^2. The solid curve corresponds to $T = 1.96$, the dashed curve to $T = 2.35$. The vertical scale shows the normalized frequencies multiplied by 1000.

variety of model atomic interactions, the Lindemann parameter at melting is about 15% of the lattice spacing.[15,16] Our calculated $\langle \delta r_q^2 \rangle^{1/2}$ for the solid[18] is 16% of the lattice spacing at $T = 1.96$ (cf. Fig. 7), and probably remains near that value up to just below $T = 2.35$. (At $T = 2.35$, the configurations begin to sample a region of the hypersurface containing a basin other than the well surrounding the crystal minimum, and the root-mean square return distance is no longer identical with the conventional Lindemann parameter.) While the Lindemann theory has proven useful, it should not be regarded as a comprehensive theory of melting, even where it is exact, for it says nothing about the coexisting liquid phase.[16] Indeed, the Lindemann parameter, as originally conceived, is not even defined in the liquid because of diffusion. Our return distance parameter is on the one hand identical to the Lindemann parameter when the configurations remain in the neighborhood of the crystal minimum, and on the other hand is well defined in the liquid phase. The return distance parameter opens up the possibility of developing a truly "two-sided" theory of melting which acknowledges the properties of both the liquid and solid phases. A generalized Lindemann criterion along these lines, based upon the information presented in Fig. 7, might be that the solid melts when $\langle \delta r_q^2 \rangle^{1/2}$ reaches 15% of the lattice spacing, and the melt freezes when $\langle \delta r_q^2 \rangle^{1/2}$ declines to about three times that value. Ours is not the first attempt to generalize the Lindemann parameter to the liquid phase. Ashcroft and co-workers, in their studies of liquid metals, regard the hard-sphere packing fraction as the Lindemann parameter for liquids.[19] They have developed a successful first-principles theory of the melting of sodium which incorporates this point of view.[20] They suggest that the liquid counterpart to the Lindemann criterion is that the liquid freezes when the hard-sphere packing fraction drops to 0.42. While such an approach seems reasonable for spherical atomic liquids if an appropriate hard-sphere diameter can be assigned, we do not expect to see its application to nonspherical molecular substances. However, our return distance parameter is not only more directly connected to the Lindemann parameter, but is also not limited to spherical atomic substances.[21] Of course, a Lindemann-like rule for the freezing of liquids has not yet been generally established even for atomic liquids. However, neither this lack nor the apparent failure of the conventional Lindemann picture of melting for molecular solids[17] rules out the development of a generalized Lindemann rule for the freezing of liquids.

Perhaps the most important use that we can make of the return distance parameter is in a defect-mediated theory of melting. The return distance parameter clearly signals the appearance and importance of defective inherent structures at and above T_m. In the case studied here, the defects seem to be only simple variations of a vacancy-interstitial pair. A simple theory of melting based upon the presence and energetic details of vacancy-interstitial pairs of defects has already proved successful for a model sodium solid.[22] The evidence presented here suggests that we can expect some version of such theories to enjoy broader success. Of course,

the techniques presented here would apply equally well if the melting had been preceded by, say, inherent structures with extended dislocations rather than point defects. Therefore, we expect that we can apply these general geometric techniques to study melting even apart from the question of validity of specific defect-mediated theories.

ACKNOWLEDGMENT

[1]F. H. Stillinger and T. A. Weber, Science **225**, 983 (1984).

[2]J. -P. Hansen and I. R. McDonald, *Theory of Simple Liquids* (Academic, London, 1976), Chap. 3.

[3]F. H. Stillinger and T. A. Weber, Phys. Rev. A **28**, 2408 (1983).

[4]J. O. Hirschfelder, C. F. Curtiss, and R. B. Bird, *Molecular Theory of Gases and Liquids* (Wiley, New York, 1954), p. 1041.

[5]C. W. Gear, *Numerical Initial-Value Problems in Ordinary Differential Equations* (Prentice–Hall, Englewood Cliffs, 1971).

[6]We designate the average calculated temperature with T, according to custom, rather than with the more consistent but unusual $\langle T \rangle$.

[7]See Ref. 2, p. 363.

[8]To see this, write $\langle \mathrm{tr} \nabla\nabla U \rangle$ as the canonical configurational average $\frac{1}{Z}\int d\mathbf{r}_1 \dots d\mathbf{r}_N \exp(-U/k_B T)\mathrm{tr}\,\nabla\nabla U$. Integrate the numerator by parts, discarding the surface term which vanishes in the thermodynamic limit, to find $\langle \mathrm{tr}\,\nabla\nabla U \rangle = (k_B T)^{-1}\langle |\nabla U|^2 \rangle$. In our units, $k_B = 1$. See Sec. 6.10 of Ref. 2 for the traditional application of this equality to the development of the Wigner-Kirkwood quantum-mechanical corrections to classical thermodynamics.

[9]This generalization has been exploited in another context. See S. Hess, Physica A **127**, 509 (1984).

[10]L. K. Moleko and H. R. Glyde, Phys. Rev. B **27**, 6019 (1983); **30**, 4215 (1984).

[11]As noted in the Introduction, in the harmonic regime $\langle \delta r_q^2 \rangle^{1/2}$ is identical with the root-mean square displacement of the coordinates from the static crystal lattice, and increases with $T^{1/2}$. See Ref. 2, p. 365.

[12]One quantitative test of how well P_E fits the data is given by the Pearson χ^2 test, where $\chi^2 = N_s \sum_{i=1}^{N(B)} [P_E(r_i^2) - P(r_i^2)]^2 / P_E(r_i^2)$, and where N_s is the sample size and $N(B)$ is the number of bins of r_i^2. Roughly, $P_E(r_i^2)$ fits the data if $\chi^2 < N(B)$. See, for example, B. L. van der Waerden, *Mathematical Statistics* (Springer, New York, 1969), Chap. 11. In our calculations, $N_s = 25\,600$ and $10 < N(B) < 100$, the number of bins of r_i^2 increasing with temperature (adjusted so that nearly all bins contain at least five samples). At $T = 1.96$, χ^2 is less than one-half $N(B)$, so $P_E(r_2)$ is an excellent fit to the data $P(r^2)$, while at $T = 2.35$, χ^2 is several times $N(B)$.

[13]For similar results with other potentials, see F. H. Stillinger and T. A. Weber, J. Chem. Phys. **80**, 4434 (1984); T. A. Weber and F. H. Stillinger, *ibid.* **81**, 5089 (1984).

[14]J. M. Ziman, *Models of Disorder* (Cambridge University, Cambridge, 1979), pp. 70–78.

[15]Sections 10.5 and 10.6 of Ref. 2.

[16]M. Ross, Phys. Rev. **184**, 233 (1969).

[17]G. H. Wolf and R. Jeanloz, J. Geophys. Res. B **89**, 7821 (1984).

[18]The error in estimating $\langle \delta u^2 \rangle$ due to the finite size of the system has been claimed to be of order $N^{-1/3}$. See W. G. Hoover, S. G.Gray, and K. W. Johnson, J. Chem. Phys. **55**, 1128 (1971).

[19]N. W. Ashcroft and D. C. Langreth, Phys. Rev. **159**, 500 (1967).

[20]D. Stroud and N. W. Ashcroft, Phys. Rev. B **5**, 371 (1972).

[21]F. H. Stillinger and T. A. Weber, Phys. Rev. B **31**, 5262 (1985).

[22]F. H. Stillinger and T. A. Weber, J. Chem. Phys. **81**, 5095 (1984).